The Astrophysical Journal, 757:115 (12pp), 2012 October 1 doi:10.1088/0004-637X/757/2/115

DELAYED ONSET OF HIGH-ENERGY EMISSIONS IN LEPTONIC AND HADRONIC MODELS OF GAMMA-RAY BURSTS

Katsuaki Asano[1] and Peter Mészáros[2]
[1] Interactive Research Center of Science, Tokyo Institute of Technology, 2-12-1 Ookayama, Meguro-ku, Tokyo 152-8550, Japan; asano@phys.titech.ac.jp
[2] Department of Astronomy and Astrophysics, Department of Physics, Center for Particle and Gravitational Astrophysics, Pennsylvania State University, University Park, PA 16802, USA; nnp@astro.psu.edu
Received 2012 May 31; accepted 2012 August 5; published 2012 September 10

ABSTRACT

The temporal–spectral evolution of the prompt emission of gamma-ray bursts is simulated numerically for both leptonic and hadronic models. For weak enough magnetic fields, leptonic models can reproduce the few seconds delay of the onset of GeV photon emission observed by *Fermi*-LAT, due to the slow growth of the target photon field for inverse Compton scattering. For stronger magnetic fields, the GeV delay can be explained with hadronic models, due to the long acceleration timescale of protons and the continuous photopion production after the end of the particle injection. While the FWHMs of the MeV and GeV light curves are almost the same in one-zone leptonic models, the FWHMs of the 1–30 GeV light curves in hadronic models are significantly wider than those of the 0.1–1 MeV light curves. The amount of the GeV delay depends on the importance of the Klein–Nishina effect in both the leptonic and hadronic models. In our examples of hadronic models the energies of the escaped neutrons are comparable to the gamma-ray energy, although their contribution to the ultra high-energy cosmic rays is still subdominant. The resulting neutrino spectra are hard enough to avoid the flux limit constraint from IceCube. The delay of the neutrino emission onset is up to several times longer than the corresponding delay of the GeV photon emission onset. The quantitative differences in the light curves for various models may be further tested with future atmospheric Cerenkov telescopes whose effective area is larger than that of *Fermi*-LAT, such as CTA.

Key words: cosmic rays – gamma-ray burst: general – neutrinos – radiation mechanisms: non-thermal

Online-only material: color figures

1. INTRODUCTION

The nature of the prompt emission mechanism of gamma-ray bursts (GRBs) is still controversial, and remains a challenging problem in high-energy astrophysics. Most of the GRB spectra peak around the 0.1–1 MeV range, and on the whole are well fitted by the Band function (Band et al. 1993). In the standard picture, this component is explained by synchrotron emission from accelerated electrons in a generic dissipation region (Piran 2005; Mészáros 2006) outside the photosphere but inside the external shock radius. However, alternative models have been proposed such as photospheric emission (see, e.g., Rees & Mészáros 2005; Giannios 2007; Beloborodov 2010; Ryde et al. 2010). The recent detection of GeV photons with *Fermi*-LAT has opened up the possibility of constraining such models. In some objects *Fermi* has also found in the GeV energy range additional spectral components (Abdo et al. 2009a, 2009b; Ackermann et al. 2010, 2011). Moreover, a general feature is that the onset of the GeV emission tends to be delayed relative to the onset of the main MeV emission (Abdo et al. 2009c; and others including the above references). The typical delay timescales for the long *Fermi*-LAT GRBs are 3–5 s as seen in GRB 080916C, GRB 090902B, and GRB 090926A (Mészáros 2012). The simplest model to explain this would be inverse Compton emission from the same internal dissipation region as the MeV (Corsi et al. 2010; Asano & Mészáros 2011, hereafter AM11). A hadronic origin for the GeV emission has also been proposed (Asano et al. 2009a, 2010; Razzaque et al. 2010), although such models require a much larger energy in accelerated protons than in the emitted gamma-ray energy. Alternatively, if the Lorentz factor of the external shock propagating in the interstellar medium is as high as 1000, the delayed onset of the GeV emissions may be attributed (Ghisellini et al. 2010; Kumar & Barniol Duran 2010) to an early onset of a forward shock synchrotron afterglow. Other mechanisms to reproduce the GeV delay are proposed by several authors (see, e.g., Toma et al. 2009; Ioka 2010), but we have not arrived at an established interpretation yet.

The photon statistics above the GeV range provided by *Fermi* are not sufficient to distinguish between the internal and external origin of the high-energy emission. However, it is expected that future multi-GeV observations with atmospheric Cerenkov telescope arrays such as CTA (Gilmore et al. 2012; Kakuwa et al. 2012; Inoue et al. 2012) will drastically improve the data quality, owing to their large effective area. Light curves and spectral evolution determinations expected from such telescopes should provide critical information on the GRB physics, currently being pioneered by *Fermi*. To discriminate between the emission models, detailed temporal–spectral evolution studies for various situations (e.g., Pe'er & Waxman 2005; Pe'er 2008; Belmont et al. 2008; Vurm & Poutanen 2009; Bošnjak et al. 2009; Daigne et al. 2011) are needed.

In this paper, we concentrate on the internal dissipation regions as possible models for explaining the delayed onset of the GeV emission. In AM11, we developed a time-dependent code that can follow the evolution of the particle energy distributions in a relativistically expanding shell with Lorentz factor Γ and initial radius R_0 from the central engine. In this previous AM11 calculation we included only leptonic processes. However, GRBs have been considered as possible sources of ultra high-energy cosmic rays (UHECRs; Waxman 1995; Vietri 1995), and the electromagnetic cascades initiated by photopion production from accelerated protons (hadronic cascade; Böttcher & Dermer 1998; Gupta & Zhang 2007) result in both neutrinos and very high energy photons. The latter, potentially, could reproduce the delayed onset of the GeV emission observed, because of the long proton-acceleration timescale and/or the continuous pion production even after the end of particle injection. Also, the flat spectrum of the keV–GeV power-law component seen in GRB 090902B (Abdo et al. 2009b) is compatible with a hadronic cascade model (Asano et al. 2010). Thus, in order to explore the time evolution of hadronic models, in this paper we incorporate the full details of the hadronic processes into the time-dependent code from AM11. With this expanded code, we are able to calculate the time evolution of the usual leptonic model, as well as the time evolution of the radiation from hadronic cascade models.

The observed light curves can show several pulses, and the origin of the time variability timescale is unknown. One possibility for this is variability in the central engine ejection, in which case the observed pulse widths are limited by the usual formula $\sim R_0/c\Gamma^2$, and there could be multiple MeV-photon sources before the GeV onset. In this case, the GeV delay is due to a superposition of the effects from various shell sources with different model parameters, the first pulse tending to have a soft spectrum in this scenario. Alternatively, the variability might be due other effects, such as hydrodynamical turbulence in the shell or behind the shocks (Kumar & Narayan 2009; Zhang et al. 2009; Mizuno et al. 2011; Inoue et al. 2011), with various unconstrained parameters. To avoid such model-dependent uncertainties, in this paper we restrict ourselves to the study of a single primary pulse produced in a one-zone model, our code producing a smooth light curve, which can be considered as an envelope which averages a possible underlying variability with some smoothing. What we test is whether a single pulse in such a one-zone model can reproduce the observed GeV delays or not, with either leptonic or hadronic radiation mechanisms. The differences in the light curves for the various models explored in this paper provide clues which would be useful for discriminating between them, using future observations from atmospheric Cerenkov telescopes.

In Section 2, we go into some of the details of the new numerical code for calculating the spectral evolution. The basic model features and our numerical results are presented in Section 3 for the leptonic model and in Section 4 for the hadronic model. A discussion and summary of these results is given Section 5.

2. NUMERICAL METHODS

The numerical code in this paper is developed from the one-zone code in AM11. With this code we can simulate the temporal evolution of photon emission. The photon source in this code is a shell expanding with the Lorentz factor Γ from an initial radius $R = R_0$. This shell is responsible for one pulse, as part of a light curve which may have multiple pulses. The calculation of the photon production (for details see AM11) is carried out in the shell frame (hereafter, the quantities in this frame are denoted with primed characters). In this paper we express particle kinetic energies of electrons, protons, and photons as $\varepsilon_{\rm e} = (\gamma_{\rm e}-1)m_{\rm e}c^2$, $\varepsilon_{\rm p} = (\gamma_{\rm p} - 1)m_{\rm p}c^2$ and ε, respectively.

The code used in AM11 can simulate the injection and cooling for electrons/positrons, and production, absorption, and escape for photons with physical processes of (1) synchrotron, (2) Thomson or inverse Compton (IC) scattering (including the Klein–Nishina regime), (3) synchrotron self-absorption (SSA), (4) $\gamma\gamma$ pair production, (5) adiabatic cooling. In the present paper, a new feature is the incorporation of the hadronic processes (based on the simulation methods in the series of GRB studies of Asano 2005, Asano & Nagataki 2006, Asano & Inoue 2007, and Asano et al. 2009b) into the code of AM11. For GRB prompt emission, the most important process in hadronic cascade is photopion production. The timescale of photopion production in the one-zone approximation is written as

$$t'^{-1}_{\rm p\gamma} = \frac{c}{2}\int d\varepsilon' \int_{-1}^{1} d\mu'(1-\mu')n'_\gamma(\varepsilon')\sigma_{\rm p\gamma}K_{\rm p\gamma}, \qquad (1)$$

where $n_\gamma(\varepsilon)$ is the energy distribution of the photon density, μ is the cosine of the photon incident angle, and $K_{\rm p\gamma}$ is the inelasticity. We adopt experimental results for the cross sections $\sigma_{\rm p\gamma}$ for $p\gamma \rightarrow n\pi^+$, $p\pi^0$, $n\pi^+\pi^0$, and $p\pi^+\pi^-$ for $\varepsilon'' \leqslant 2$ GeV (see Asano & Nagataki 2006 for details), where ε'' is the photon energy in the proton rest frame. Multi-pion production due to high-energy gamma rays far above the Δ-resonance ($\varepsilon'' \sim 300$ MeV) is not important in our simulations (Murase & Nagataki 2006), because the standard synchrotron model generates a sufficiently soft photon spectrum with the typical index of -1.5. For the pion production by $n\gamma$, we adopt the same cross sections as $p\gamma$. The inelasticity is approximated by a conventional method as

$$K_{\rm p\gamma} = \frac{1}{2}\left(1 - \frac{m_{\rm p}^2 - m_\pi^2}{s}\right), \qquad (2)$$

where s is the invariant square of the total four-momentum of the $p\gamma$ ($n\gamma$) system, and $m_{\rm p}$ is the proton mass. For the double-pion production, we approximate the inelasticity by replacing m_π with $2m_\pi$. Adopting the same Monte Carlo method as Asano (2005) or Asano & Nagataki (2006), we estimate energy loss of protons/neutrons and inject pions every time step following Equation (1).

For reference, we rewrite Equation (1) for a simple case, in which a source with the bulk Lorentz factor Γ emits photons at a radius R with a power-law spectrum $n'_\gamma(\varepsilon') \propto \varepsilon'^\alpha$ for $\varepsilon' < \varepsilon'_{\rm peak}$ and luminosity $L_{\rm L}$ (integrated below $\varepsilon_{\rm peak}$). Here, $\varepsilon_{\rm peak}$ corresponds to the spectral peak energy of the Band function. The result becomes

$$t'^{-1}_{\rm p\gamma} = \frac{(2+\alpha)L_{\rm L}}{8\pi R^2\Gamma^2}\frac{2^{1-\alpha}}{1-\alpha}\varepsilon'^{-(\alpha+2)}_{\rm peak}\gamma'^{-(\alpha+1)}_{\rm p}\int d\varepsilon'' K_{\rm p\gamma}\sigma_{\rm p\gamma}\varepsilon''^\alpha, \quad (3)$$

for

$$\gamma'_{\rm p} \gtrsim \gamma'_{\rm p,th} \equiv \frac{300\ {\rm MeV}}{\varepsilon'_{\rm peak}}. \qquad (4)$$

If we adopt the observationally typical index $\alpha = -1$, the timescale does not depend on the energy of the proton. As is well known, the photomeson production efficiency $f_{\rm p\gamma} \equiv t'_{\rm exp}/t'_{\rm p\gamma}$ is close to unity for fiducial parameter sets ($t'_{\rm exp} = R/c\Gamma$; Waxman & Bahcall 1997; Asano 2005; Murase & Nagataki 2006). The theoretically expected value $\alpha = -1.5$ in the standard synchrotron model leads to more efficient pion production for higher energy protons as $f_{\rm p\gamma} \propto \gamma_{\rm p}^{0.5}$. Additionally, the hadronic cascade may produce an even softer spectrum. Our time-dependent simulation is a powerful tool to follow the pion production rate as the photon spectrum evolves.

In terms of the Thomson optical depth $\tau_{\rm T}$, the pp reaction efficiency is $f_{\rm pp} \sim 0.05\tau_{\rm T}$ (Murase 2008). Thus, we can neglect the pp collisions in the optically thin cases in this paper. However, since our code is planned to apply also to optically thick cases in the near future, we have mounted the pp reaction on our code, as was done in Murase et al. (2012). Calculated with the numerical simulation kit Geant4 (Agostinelli et al. 2003), we provide tables for the cross section, inelasticity and pion-multiplicity for pp collision. The procedure to follow proton cooling and pion injection is the same as that for $p\gamma$ collision.

The Bethe–Heitler pair production process ($p\gamma \to pe^+e^-$) is also taken into account. The cooling and spectral pair injection rates are calculated with the cross section and inelasticity from Chodorowski et al. (1992).

In our code, neutral pions promptly decay into two gamma rays, while the cooling of charged pions before their decaying is taken into account. For charged particles, such as protons, pions, and muons, synchrotron and IC with the full Klein–Nishina cross section are included as photon production and cooling processes. The particle decays are simulated with the Monte Carlo method adopting the lifetime of pions (muons) as $2.6 \times 10^{-8}\gamma_\pi$ s ($2.2 \times 10^{-6}\gamma_\mu$ s). The energy fraction of muons at pion decay $\pi^+(\pi^-) \to \mu^+\nu_\mu(\mu^-\bar{\nu}_\mu)$ is approximated as $m_\mu/m_\pi \sim 0.76$, and the rest of the energy goes to a neutrino. On the other hand, we assume that the energy of a muon at its decay $\mu^+(\mu^-) \to e^+\nu_e\bar{\nu}_\mu(e^-\bar{\nu}_e\nu_\mu)$ will be shared equally by a positron (electron), neutrino, and antineutrino. We neglect neutron decay, whose timescale is much longer than all the timescales we consider in this paper.

We also take into account the effect of adiabatic cooling for charged particles with the same method in AM11. This effect is controlled by the expansion law of the volume $V' = 4\pi R^2 W'$, where W is the shell width. The volume expansion law affects the escape rate for neutral particles. As mentioned in AM11, the escape fraction of photons per unit time is $c/2W'$. We consider several cases for the expansion law in our simulations.

Assuming the jet opening angle of $\theta_{\rm jet} = 10/\Gamma$, the photon spectrum evolution for an observer is calculated in the same manner in AM11. The energy and escape time of photons coming from a surface with an angle θ (measured from the central engine, $\theta = 0$ corresponds to the line of sight) are transformed into energy and time bins in the observer's frame as $\varepsilon = \delta\varepsilon'/(1+z)$ (δ is the Doppler factor) and

$$t_{\rm obs} = (1+z)[(1-\beta_{\rm sh}\cos\theta)\Gamma t' + R_0(1-\cos\theta)/c], \quad (5)$$

respectively. When $\cos\theta < \beta_{\rm sh} \equiv \sqrt{1-1/\Gamma^2}$, photons are coming from the backside of the shell with an extra "time delay" due to the shell thickness,

$$\Delta t_{\rm ex} = (1+z)\frac{W'\Gamma}{c}\left[\left(\beta_{\rm sh}^2 + 1/\Gamma^2\right)\cos\theta - \beta_{\rm sh}\right], \quad (6)$$

relative to the emission from the front side.

The photon absorption due to extragalactic background light (EBL) is estimated by accumulating the optical depth between the source and observer with the EBL model of Kneiske et al. (2004) (best fit).

3. LEPTONIC MODELS

3.1. Delayed Inverse Compton

Inverse Compton emission, which may dominate the GeV energy range, needs low-energy seed photons. In the synchrotron self-Compton model (SSC), the seed photons are synchrotron photons emitted from power-law-distributed electrons. The growth timescale of the synchrotron photon field may explain the delay timescale of the GeV onset (Bošnjak et al. 2009). This possibility was tested by time-dependent simulations in AM11. They showed that a very low magnetic field ($\epsilon_B/\epsilon_e \sim 10^{-3}$ and $R_0 = 6\times10^{15}$ cm in their example) is required to reproduce the GeV delay. Here, we write the magnetic field

$$B' = \sqrt{\frac{2\epsilon_B L_{\rm iso}}{\epsilon_e c R^2\Gamma^2}} \quad (7)$$

$$\simeq 320\left(\frac{\epsilon_B/\epsilon_e}{10^{-3}}\right)^{1/2}\left(\frac{\Gamma}{800}\right)^{-1} \times\left(\frac{R}{10^{15}\ {\rm cm}}\right)^{-1}\left(\frac{L_{\rm iso}}{10^{54}\ {\rm erg\ s^{-1}}}\right)^{1/2}\ {\rm G}. \quad (8)$$

The standard synchrotron model attributes the spectral peak energy $\varepsilon_{\rm peak}$ to the typical photon energy emitted from the lowest-energy electrons at injection. The physical mechanism that determines the minimum Lorentz factor $\gamma_{\rm e,min}$ of those electrons is still under discussion. In a low magnetic field as given in Equation (8), to emit synchrotron photons in the MeV range, a very high minimum Lorentz factor ($\gg m_{\rm p}/m_{\rm e}$) is required as

$$\gamma'_{\rm e,min} \sim \sqrt{\frac{\varepsilon_{\rm peak} m_e c}{\hbar e B'\Gamma}} \quad (9)$$

$$\simeq 1.8\times10^4\left(\frac{\varepsilon_{\rm peak}}{\rm MeV}\right)^{1/2}\left(\frac{\epsilon_B/\epsilon_e}{10^{-3}}\right)^{-1/4} \times\left(\frac{R}{10^{15}\ {\rm cm}}\right)^{1/2}\left(\frac{L_{\rm iso}}{10^{54}\ {\rm erg\ s^{-1}}}\right)^{-1/4}, \quad (10)$$

where we have omitted the cosmological redshift factor. In this case the typical photon energy in the electron rest frame becomes

$$\varepsilon''_{\rm peak} \sim \gamma'_{\rm e,min}\varepsilon'_{\rm peak} = \gamma'_{\rm e,min}\varepsilon_{\rm peak}/\Gamma \quad (11)$$

$$\simeq 23\left(\frac{\varepsilon_{\rm peak}}{\rm MeV}\right)^{3/2}\left(\frac{\epsilon_B/\epsilon_e}{10^{-3}}\right)^{-1/4}\left(\frac{\Gamma}{800}\right)^{-1} \times\left(\frac{R}{10^{15}\ {\rm cm}}\right)^{1/2}\left(\frac{L_{\rm iso}}{10^{54}\ {\rm erg\ s^{-1}}}\right)^{-1/4}\ {\rm MeV}, \quad (12)$$

which largely exceeds $m_e c^2$, so the Klein–Nishina effect is crucial to emit IC photons. The IC photon production is an inefficient process so that the GeV component shows a slow growth compared to synchrotron. Soft photons ($\varepsilon \ll \varepsilon_{\rm peak}$) that can efficiently interact with electrons of $\gamma_{\rm e,min}$ are produced by electrons that have already undergone energy losses and have $\gamma_e < \gamma_{\rm e,min}$. However, as soft photons increase, the newly injected electrons cool via mainly IC emission owing to a very low ϵ_B/ϵ_e. Therefore, the synchrotron component starts decreasing while the IC component grows. This enhances the difference in the peak times of the MeV and GeV light curves.

For the purposes of comparison with the leptonic calculations in the present paper, we summarize here some of the leptonic results in AM11. The light curves in Figure 12 in AM11 show a GeV delay due to the mechanism we mentioned above. However, the difference in the peak times is within a pulse timescale, $\sim R/c\Gamma^2$ (the difference in the peak times is roughly half of this timescale in the example in AM11), and the GeV and 100 keV light curves converge in the late stages. The FWHMs of the two light curves are almost the same. The example in

AM11 adopted an ideal set of parameters for the GeV delay, and it seems difficult to produce even larger delays by simple SSC models. We did not find significant GeV delays for more conservative SSC parameter sets in our simulations in AM11.

An external inverse Compton (EIC) model (Beloborodov 2005; Toma et al. 2009, 2010; Li 2010; Murase et al. 2011) was also tested in AM11. The MeV photons are emitted from a smaller radius, and they are upscattered by non-thermal electrons in an outer region, where some dissipation mechanism, such as internal shocks, injects those electrons. In this model, we require two different origins for the MeV and GeV components. A GeV delay larger than the typical pulse timescale ($R/c\Gamma^2$) appears naturally, although the model requires a large number of accelerated electrons, which leads to an energy-budget problem. If the numbers of electrons and protons are the same, most of the energy carried by the protons remains unreleased. Some GRBs, in which the main MeV component is hard to explain by the usual synchrotron model, like GRB 090902B (Abdo et al. 2009b; Ryde et al. 2010; Zhang et al. 2011), are interesting applications for this model. In the frame of the outer dissipation region, the photon field coming from an inner region is highly beamed along the radial direction. The $e\gamma$-scattering probability becomes highest for head-on collision so that the scattered IC photons tend to propagate with a large angle to the radial axis. As a result, the intensity of the scattered photons becomes anisotropic. In this case, the emission from off-axis regions ($\theta \gtrsim 1/\Gamma$) contributes considerably. AM11 showed that the GeV light curve has a long tail (see Figure 15 in AM11), which is a characteristic feature of this model.

3.2. Opacity Evolution in the Leptonic Model

As a shell expands, the photon density decreases so that the opacity against $\gamma\gamma$ absorption also decreases with time. This effect may cause a gradual increase of the $\gamma\gamma$ cutoff energy (Granot et al. 2008). In this section, we test the evolution of the $\gamma\gamma$ opacity as a possible mechanism of the GeV delay. When the electron injection timescale is comparable to or shorter than the shell expansion timescale $t'_{\rm exp} = R_0/\Gamma c$, the opacity evolution tends to cause a negative GeV delay: the GeV emission is terminated earlier than the MeV emission as shown in Figure 3 or 8 in AM11. As the electron injection builds up the photon density, $\gamma\gamma$ optical depth increases, and GeV photons begin to be absorbed. It was hard to observe the effect of the opacity decrease in our simulations with an injection timescale of $R_0/\Gamma c$. Therefore, here we adopt a very long electron injection to see the opacity decay as the shell expands.

We consider a shell expanding from an initial radius $R_0 = 10^{15}$ cm with a bulk Lorentz factor $\Gamma = 500$, and optimize parameters to observe the opacity effects as below. If we take a standard assumption for the shell width as $W' = R_0/\Gamma$, the photon escape timescale and shell expansion timescale become comparable. In such a case, the opacity evolution may be softened by residual photons generated earlier but before escape. So we assume a thin shell $W' = R_0/10\Gamma$. The electron injection continues until $R = 10^{16}$ cm ($t'_{\rm inj} = 9t'_{\rm exp}$) with a constant rate, and its isotropic-equivalent energy for this pulse is $E_{\rm e,pls} = 2 \times 10^{54}$ erg. The injection spectrum is assumed as a cutoff power-law shape, $\dot{N}'_{\rm e,inj}(\varepsilon'_{\rm e}) \propto \varepsilon'^{-p_{\rm e}}_{\rm e} \exp(-\varepsilon'_{\rm e}/\varepsilon'_{\rm e,max})$ for $\varepsilon'_{\rm e} > \varepsilon'_{\rm e,min}$, where $\varepsilon'_{\rm e,max}$ is determined by equating the cooling timescale $t'_{\rm cool}$ (synchrotron, IC, and SSA are taken into account)

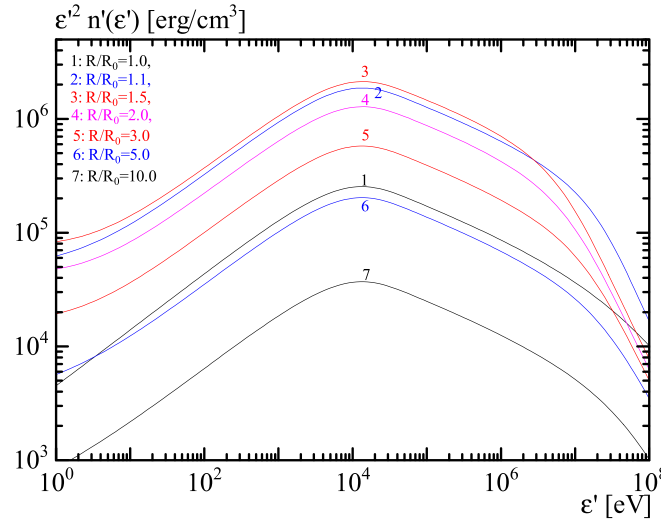

Figure 1. Opacity evolution in the leptonic model: spectral evolution of photon density in the shell frame with the expanding radius R (see the text in Section 3.2). Initially the photon density increases as electrons are injected ($R < 1.5\ R_0$), then the shell expansion and photon escape make the density begin to decrease. In this stage, the break energy $\varepsilon'_{\rm br} \sim 10^7$ eV due to $\gamma\gamma$ absorption gradually grows as the shell expands.

(A color version of this figure is available in the online journal.)

and the acceleration timescale

$$t'_{\rm acc} = \xi \frac{\varepsilon'_{\rm e}}{ceB'}. \qquad (13)$$

In this section we assume the electron index $p_{\rm e} = 2.5$, and "Bohm limit" acceleration as $\xi = 1$. In order to avoid contamination of other evolutionary effects, the magnetic field $B' = 3.9 \times 10^4$ G, shell width, and minimum injection energy of electrons $\varepsilon'_{\rm e,min} = 2$ GeV are assumed to be constant during the electron injection. However, the ratio $\epsilon_B/\epsilon_{\rm e}$, which may be approximated as

$$\frac{\epsilon_B}{\epsilon_{\rm e}} \simeq \frac{B'^2}{8\pi}\left(\frac{1}{4\pi R^2 W'}\frac{E_{\rm e,pls}}{\Gamma}\frac{t'_{\rm esc}}{t'_{\rm inj}}\right)^{-1} = \frac{9R_0R^2\Gamma B'^2}{2E_{\rm e,pls}}, \qquad (14)$$

evolves from 0.04 to 4 during the electron injection.

Figure 1 shows the spectral evolution in the shell frame. The spectral peak energy $\varepsilon'_{\rm peak} \sim 10$ keV arising from the parameter set chosen here is somewhat higher than the usual values. This is because we are considering a special case similar to GRB 080916C, which showed a delayed GeV onset with a source-frame peak energy of $(1+z)\varepsilon_{\rm peak,obs} \sim 6$ MeV (Abdo et al. 2009c). In a strict sense, $R = R_0$ in Figure 1 means that a short time $t'_{\rm exp}/100$ has passed after the electron injection started. At this point, the spectrum is not in a steady state for photon production, escape, and $\gamma\gamma$ absorption. During the initial phase for $R \leqslant 1.5\ R_0$, the opacity still increases with the photon density. At $R = 1.5\ R_0$ the high-energy portion of the spectrum can be approximated by a broken power law with a photon index $\beta \sim -2.3$ below the break energy $\varepsilon'_{\rm br}$ and -3.3 above that, rather than an exponential cutoff. This break is similar to the prediction by Granot et al. (2008), in which a thin slab is considered as a photon source. However, the mechanism for yielding a broken power law is different for our one-zone model with a finite shell width. In a quasi-steady state, the fraction of photons, whose annihilation timescale $t'_{\rm ann}$ is shorter than the escape timescale

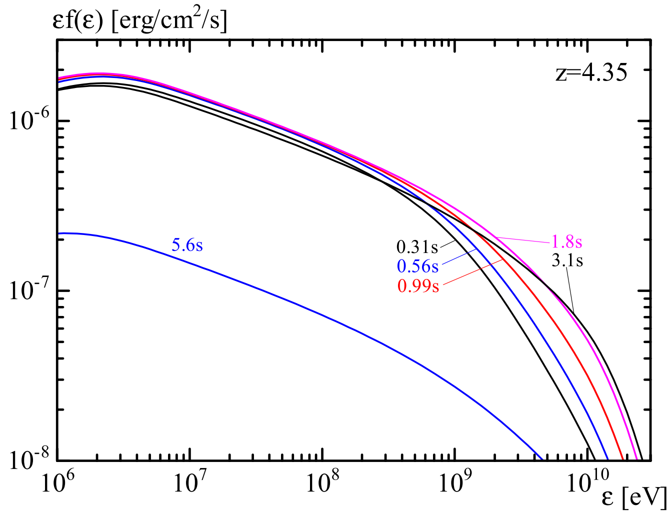

Figure 2. Opacity evolution in the leptonic model: flux evolution for an observer with $z = 4.35$ (see the text in Section 3.2).

(A color version of this figure is available in the online journal.)

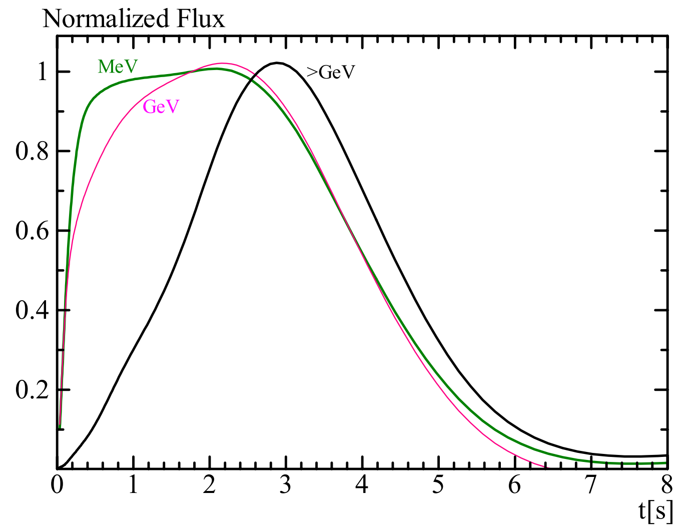

Figure 3. Opacity evolution in the leptonic model: light curve (see the text in Section 3.2). The source redshift is assumed to be 4.35. The lines labeled with "GeV" or "MeV" are plotted based on the spectral flux, while the line labeled with ">GeV" is a curve based on the photon number integrated above GeV.

(A color version of this figure is available in the online journal.)

$t'_{\rm esc} \sim W'/c$, may be written as $t'_{\rm ann}/t'_{\rm esc}$. Then, the spectral shape may be $n'_0(\varepsilon')t'_{\rm ann}/t'_{\rm esc}$, where $n'_0(\varepsilon') \propto \varepsilon'^{\beta}$ is the intrinsic spectrum, whose density is determined by the balance between continuous photon production and escape/volume expansion without the absorption effect. The annihilation timescale is $t'_{\rm ann} \propto \varepsilon'^{\beta+1}$ (Lithwick & Sari 2001; Asano & Takahara 2003), while $t'_{\rm esc}$ is independent of the photon energy. Therefore, $n'(\varepsilon') \propto \varepsilon'^{2\beta+1}$ above the spectral break at $\varepsilon'_{\rm br} \sim 10^7$ eV. The value $\beta \sim -2.3$ implies that the index should be -3.6. We should note that photons above $\varepsilon' > 10^7$ eV interact with photons below $\varepsilon'_{\rm peak}$. In our example in Figure 1, the index of the photon distribution for one order of magnitude just below $\varepsilon'_{\rm peak}$ is $\alpha \sim -1.3$. In such cases, the spectrum should be $n'(\varepsilon') \propto \varepsilon'^{\beta+\alpha+1} \sim \varepsilon'^{-3.0}$. Our result seems consistent with those estimates.

In the later stage ($R \geqslant 2\,R_0$), the $\gamma\gamma$ attenuation gradually becomes inefficient, and this causes the photon spectral break energy to increase with time. In this stage the photon distribution may be in the quasi-steady state. Therefore, the spectra for $R = R_0$ (photon-density growing stage) and $R = 5\,R_0$ are different in spite of their similar photon densities. The deviation from a simple power law seen around 1 eV is due to electron heating via SSA (Ghisellini et al. 1988, AM11).

Assuming a source redshift $z = 4.35$ such as that of GRB 080916C, we show the evolution of the spectrum for an observer in Figure 2. Given a luminosity $L_{\rm H}$ above $\varepsilon_{\rm peak}$, in a case of the usual short electron-injection ($t'_{\rm inj} \leqslant R_0/\Gamma c$), an analytical estimate (Lithwick & Sari 2001; Asano & Takahara 2003) gives us the $\gamma\gamma$ cutoff/break energy as

$$\varepsilon_{\gamma\gamma} = \frac{m_{\rm e}^2 c^4}{\varepsilon_{\rm peak}} \Gamma^{2\frac{\beta-1}{\beta+1}} \left[\frac{\sigma_{\rm T} L_{\rm H}}{16\pi \varepsilon_{\rm peak} c^2 \delta t} F(\beta) \right]^{\frac{1}{\beta+1}} \propto \delta t^{-\frac{1}{(\beta+1)}}, \quad (15)$$

where the dimensionless function $F(\beta) \sim 10^{-2}$, and $\delta t = R/\Gamma^2 c$ is the variability timescale. For our continuous injection case, that may be interpreted as $\varepsilon_{\gamma\gamma} \propto t_{\rm obs}^{0.8}$ with $\beta = -2.3$. By comparing spectra for $t_{\rm obs} = 0.31$ s and 3.1 s, we can see that the spectral behavior is close to this analytical approximation; the break energy grows by a factor of six or more.

However, the spectral shape does not show a sharp cutoff or break. The deviation from the extrapolation of the low-energy spectral shape is gradual. As a result, the spectral flux at GeV (see "GeV" in Figure 3) shows a similar evolution to the flux at MeV. The MeV light curve has a plateau reflecting the constant electron injection rate. The peak time of the GeV light curve is delayed relative to the MeV rising time, but the GeV flux changes slowly during the MeV plateau phase. However, for low photon statistics, the light curve would be obtained by accumulating photon counts above GeV. As shown in Figure 3, the light curve based on the accumulated photon counts shows a distinct delay relative to the MeV light curve.

We have considered an artificial setup to see a GeV delay due to the opacity evolution. Even in this extreme case, the spectral evolution is gradual, and it seems different from the observed "sudden" onset of GeV emission.

4. HADRONIC MODELS

The electromagnetic cascade triggered by photopion production can make GeV extra components as shown in our series of GRB studies (Asano & Inoue 2007; Asano et al. 2009a, 2009b, 2010). The electron cooling timescale is much shorter than the timescales of proton acceleration and photopion production. Those timescales and continuous photomeson production after the end of electron injection may cause a delayed onset of the GeV emission.

In this section, we inject electrons and protons with the same timescale $t'_{\rm inj} = R_0/\Gamma c$. The injection spectra have the same shape as that for electrons in Section 3.2. The proton injection index is assumed to be $p_{\rm p} = 2.0$, which is appropriate to make GRBs contribute to UHECRs (Waxman & Bahcall 1998), while that for electrons is taken to be $p_{\rm e} = 3.0$ to reproduce the typical photon index $\beta \sim -2.5$ measured by BATSE (Preece et al. 2000; Kaneko et al. 2006). Although the injection indices for protons and electrons are different, the energy scales we consider are largely different for electrons and protons (see Asano et al. 2009b, for further discussion). We

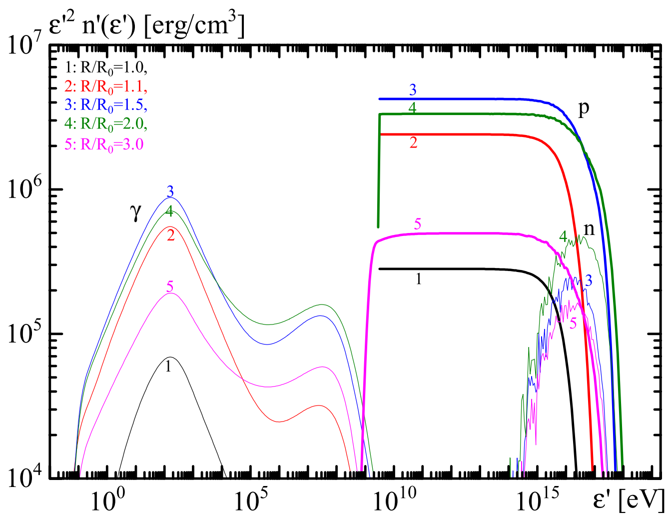

Figure 4. Hadronic model, "moderate" case: spectral evolution of the photons, protons, and neutrons in the shell frame with the expanding radius R (see the text in Section 4.1). As particle injection proceeds, the photon and proton densities build up. Then, for $R > 1.5\ R_0$, the density starts to decrease due to the effects of the shell expansion and photon escape. The electromagnetic cascade triggered by photopion production gradually enhances the height of the second peak ($\varepsilon' \sim 10^8$ eV) relative to that of the main peak ($\varepsilon' \sim 10^2$ eV) in the photon spectrum.

(A color version of this figure is available in the online journal.)

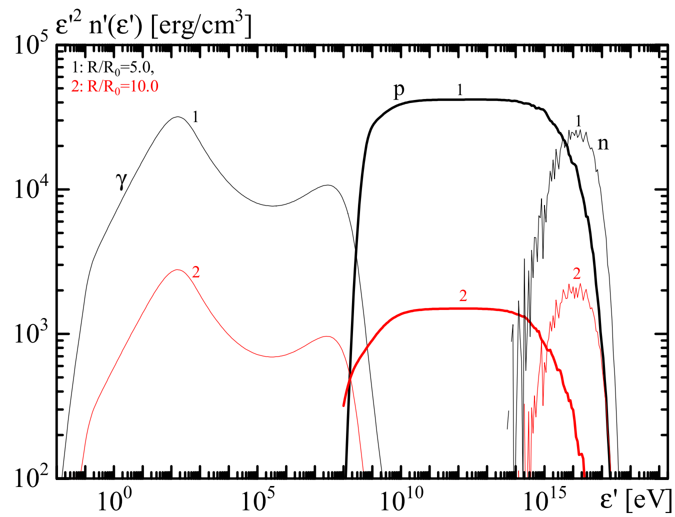

Figure 5. Hadronic model, "moderate" case: same as Figure 4 but for later stage. Neutrons, which, being neutral, are not subject to adiabatic cooling, dominate the high energy region above 10^{15} eV.

(A color version of this figure is available in the online journal.)

adopt the parameter $\xi = 1$ for both electrons and protons (see Equation (13)). The maximum energy of protons is determined by equating the cooling and acceleration timescales or by the condition that the Larmor radius should be shorter than the shell width. We take into account proton synchrotron and photopion production to estimate the cooling timescale. While the proton maximum energy at injection is controlled by the time step for injection, we phenomenologically carry out succeeding proton acceleration following the acceleration timescale and index. The minimum energy of the protons is fixed at 3 GeV.

We find that the shell width expansion enhances the GeV delay in our simulations. Below, we show examples with an expanding width as $W' = R/\Gamma$. During the particle injection, we neglect adiabatic cooling and decay of the magnetic field. After the particle injection, the magnetic field is assumed to decay as $B' \propto R^{-2}$.

In this paper the MeV photon peak is assumed to be produced by accelerated electrons injected in the emission region, which differs from the previous assumption in Asano et al. (2009a, 2010), where an ad hoc Band-type photon component matching the observed spectra was postulated. Therefore, differences from the preceding simulations arise not only because here we consider the time dependence, but also because some of the basic input assumptions are different. One issue here is that the synchrotron emission from the primarily accelerated electrons yields a soft photon index $\alpha \sim -1.5$, which is difficult for reproducing the observed spectral indices. This is because the effective energy distribution for cooled electrons below $\gamma_{\rm e,min}$ becomes $n_{\rm e}(\gamma_{\rm e}) \propto \gamma_{\rm e}^{-2}$, when the synchrotron emission is the dominant cooling process ($\dot{\gamma}_{\rm e} \propto \gamma_{\rm e}^2$). In order to resolve this contradiction, another mechanism for the Band component is required, such as a photosphere model or continuous particle acceleration by turbulence (Asano & Terasawa 2009; Murase et al. 2012). However, since our emphasis here is more on the GeV components, for simplicity we consider here the standard synchrotron model.

4.1. Hadronic "Moderate" Case

Here we adopt a typical GRB luminosity for one pulse in a GRB, as opposed to the high values deduced for LAT bursts. The model parameters are $\Gamma = 800$, $R_0 = 10^{14}$ cm, $E_{\rm e,pls} = 5.0 \times 10^{50}$ erg, and an isotropic-equivalent energy of protons $E_{\rm p,pls} = 6.1 \times 10^{51}$ erg ($\epsilon_{\rm p}/\epsilon_{\rm e} \simeq 12$)[3] including the acceleration effect after injection. The initial magnetic field B'_0 is set through the parameter ratio at $R = 2\ R_0$ as

$$\frac{\epsilon_B}{\epsilon_{\rm e}} \simeq \frac{4R_0^3 B_0'^2}{E_{\rm e,pls}} = 3.0, \tag{16}$$

which results in $B'_0 = 1.9 \times 10^4$ G. The peak energy $\varepsilon_{\rm peak}$ is adjusted to be $\sim$100 keV by adopting $\varepsilon'_{\rm e,min} = 380$ MeV.

In Figures 4 and 5, the main particle spectra are plotted in the shell frame, omitting for clarity the spectra of the electron/positron, pion, muon, and neutrino components. In the early phase ($R < 2\ R_0$), the proton density is increasing by proton injection, and their maximum energy is growing with the radius R obeying the proton acceleration timescale. Then, protons undergo adiabatic cooling, while neutrons keep their energies until they escape or interact with photons. The volume expansion ($V' \propto R^3$) reduces the particle number densities, and particle escape also affects the densities of neutrons and photons. The evolution of the neutron-to-proton ratio from 2 R_0 to 3 R_0 indicates that pion (and neutron as well) production continues even after the end of particle injection. Therefore, the electromagnetic cascade due to the photopion process continues as well for $t' > t'_{\rm inj}$.

In the photon spectra, we can see a $\gamma\gamma$ cutoff at $\sim 10^8$ eV and an SSA signature at $\sim$0.1 eV. The second peak of the gamma-ray spectra at $\sim 10^8$ eV is due both to SSC by the primarily accelerated electrons and to synchrotron emission by secondary electrons/positrons. The cascade due to the photopion process raises the second peak relative to the synchrotron first peak even for $R > 2\ R_0$. At $R = 10\ R_0$, the highest energy region ($>10^{16}$ eV) is dominated by neutrons, because protons have been adiabatically cooled.

[3] An alternative notation in some papers is $1/f_e \simeq \epsilon_{\rm p}/\epsilon_{\rm e}$.

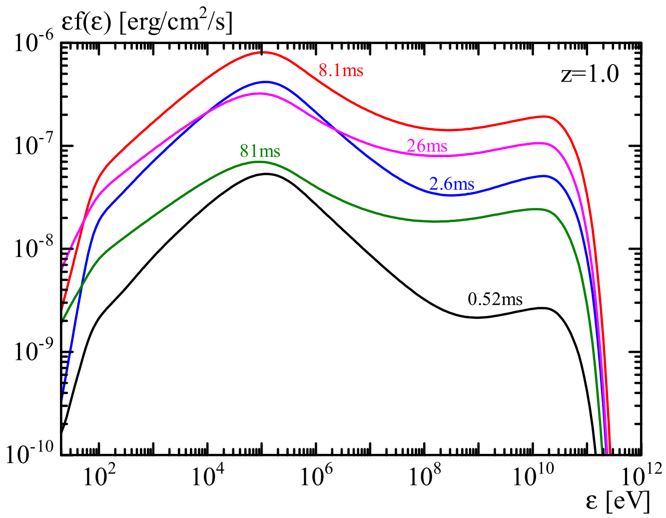

Figure 6. Hadronic model, "moderate" case: flux evolution (see the text in Section 4.1) for an observer with $z = 1$.

(A color version of this figure is available in the online journal.)

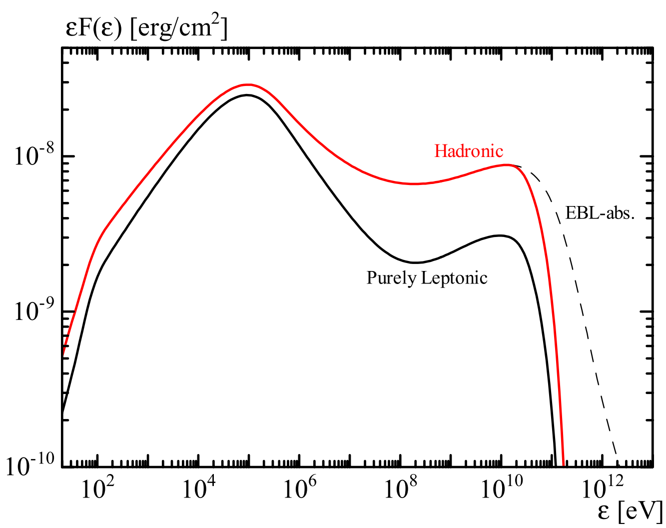

Figure 7. Fluences for the hadronic model and purely leptonic model ($\epsilon_p = 0$) with the "moderate" parameters (see the text in Section 4.1) for an observer with $z = 1$. The dashed line is the spectrum without the absorption effect of EBL.

(A color version of this figure is available in the online journal.)

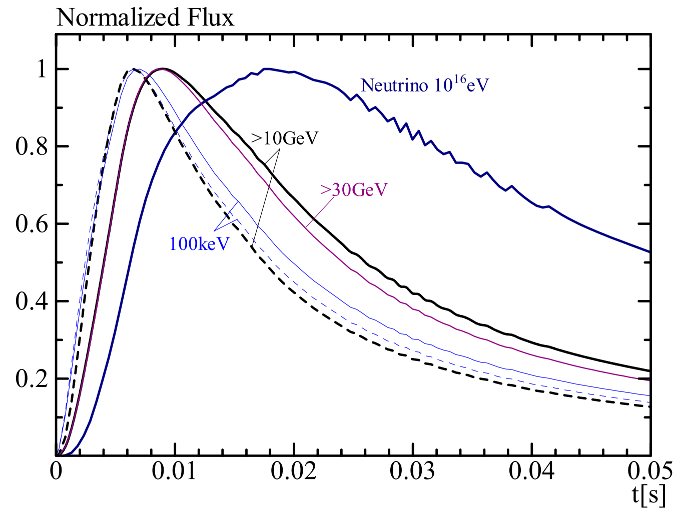

Figure 8. Light curves for the "moderate" case with $z = 1$. See the text in Section 4.1. The designation of the labels is the same as that in Figure 3. The solid lines correspond to the hadronic model, while the dashed lines are for the same leptonic model without proton injection. The neutrino flux evolution at 10^{16} eV is also plotted.

(A color version of this figure is available in the online journal.)

Assuming $z = 1.0$, we plot the spectral flux evolution of gamma rays for an observer in Figure 6. It is clearly seen that the spectral shape above $\varepsilon_{\rm peak}$ becomes harder with time, and the fraction of the GeV–10 GeV component grows. The softening in the lower energy region ($\varepsilon < \varepsilon_{\rm peak}$) is also caused by the hadronic cascade. The time-integrated spectrum is shown in Figure 7, in which we compare this hadronic model with the same (leptonic) model without proton injection. Both models show a second peak at 10^{10} eV, in the leptonic case this being due to the SSC emission, while in the hadronic it is due to the cascade. Thus, it is hard to distinguish these models just from their spectral shape. However, as shown in Figure 8, the light curves for the hadronic model (solid lines) may be distinguishable from those for the leptonic models (dashed lines). One sees that the 100 keV and 10 GeV light curves for the leptonic model (dashed lines) have almost the same shape, and the GeV delay does not appear in this leptonic case. In order to produce a GeV delay in these leptonic models, we may need a smaller magnetic field, such as $\epsilon_B/\epsilon_e < 10^{-3}$ or $B' \lesssim 100$ G, as shown in AM11. On the other hand, for the "moderate" hadronic model, the 10 GeV or 30 GeV light curves show a distinct (even if short) delay relative to the 100 keV light curve. Even so, the peak time for the 10 (30) GeV light curve is earlier than the peak time for the neutrino light curve. This may be because the SSC contribution from primary electrons is not negligible in the 10 (30) GeV light curve.

In this example, the isotropic-equivalent energies of escaped neutrinos and neutrons are 4.4×10^{49} erg and 2.2×10^{50} erg, respectively, per pulse. For reference, let us roughly estimate diffuse neutrino background and the contribution of the escaped neutrons to the UHECR flux based on this specific parameter set. Here we consider multiple pulses with the identical parameter set for a GRB. The pulse number $N = 30$ with the "moderate" parameter set yields the total isotropic-equivalent gamma-ray energy of $E_{\rm iso} = 2.0 \times 10^{52}$ erg. This energy scale can be used as a typical example. The local GRB rate ~ 1 Gpc^{-3} yr^{-1} with the average energy $E_{\rm iso} = 2.0 \times 10^{52}$ erg corresponds to the gamma-ray energy release rate of 2×10^{43} erg Mpc^{-3} yr^{-1}. The redshift $z = 1$ in this example is lower than the observed average redshift (Jakobsson et al. 2006), so the total fluence 7.4×10^{-6} erg cm^{-2} per burst is also slightly larger than the typical GRBs. Simply accumulating this identical GRB at $z = 1$ with $N = 30$ and the GRB rate of 667 yr^{-1} (Abbasi et al. 2012), we plot the spectra of the neutrino background in Figure 9. Here we have not distinguished between the neutrino species, so the spectrum consists of neutrinos originating from both pion decay and muon decay. Even though the adopted gamma-ray fluence is larger than the average one, the neutrino fluence is lower than the IceCube limit for ν_μ (Abbasi et al. 2012). This may be due to the large R_0 and Γ in this model. Furthermore, note that the dominant energy region for this model is 10^{17}–10^{18} eV, which is well above the energy region constrained with IceCube. Both in Abbasi et al. (2012) and here, the neutrino spectrum is consistent with the commonly considered case where neutrinos from pion decay dominate, in which the lower energy break of the neutrino

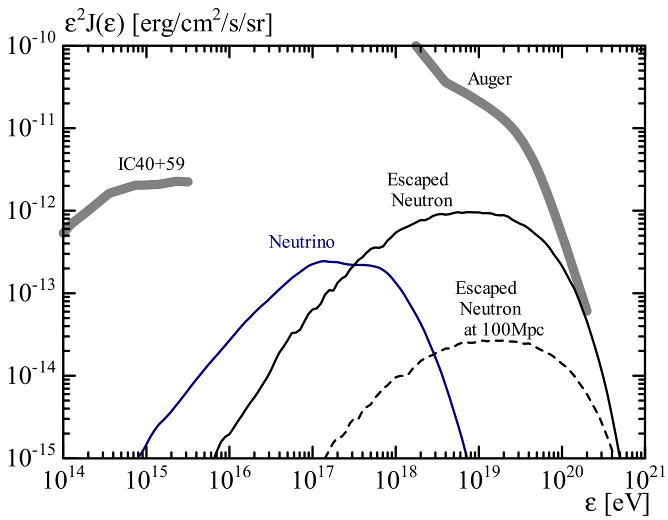

Figure 9. Spectra of the diffuse neutrons and neutrinos (without the GZK effect) adopting a model corresponding to the "moderate" case ($\epsilon_p/\epsilon_e \simeq 12$), from $z = 1$ (full lines, accumulating 667 GRBs yr^{-1}), and from 100 Mpc (dashed line, for neutrons with a local rate 2 GRBs Gpc^{-3} yr^{-1}); see the text in Section 4.1. The upper limit for ν_μ derived by IceCube (Abbasi et al. 2012) and the UHECR flux determined by the Auger team (Abraham et al. 2010) are also plotted.

(A color version of this figure is available in the online journal.)

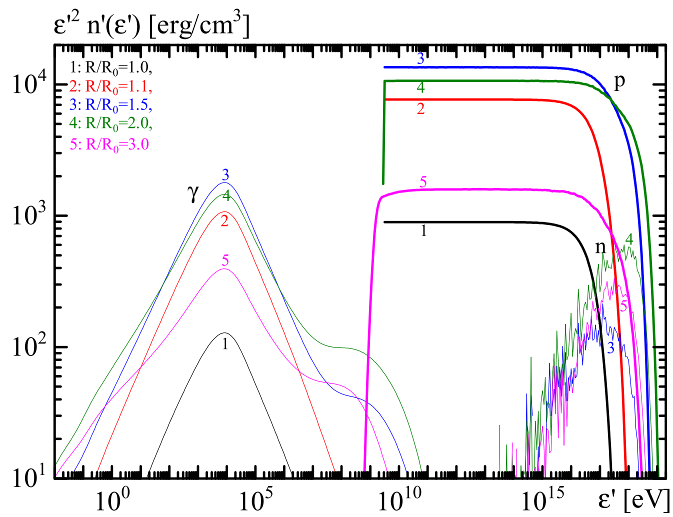

Figure 10. Hadronic "*Fermi*-LAT" case: spectral evolutions for photons, protons, and neutrons in the shell frame with the expanding radius R (see the text in Section 4.2). The bump in the photon spectra at 10^7–10^{10} eV is due purely to hadronic cascades.

(A color version of this figure is available in the online journal.)

spectrum (Waxman & Bahcall 1997) is given by

$$\varepsilon_{\nu,\mathrm{br}} \simeq \left(1 - \frac{m_\mu}{m_\pi}\right) K_{p\gamma} \gamma'_{p,\mathrm{th}} \delta \tag{17}$$

$$\simeq 8.6 \times 10^{16} \left(\frac{1+z}{2}\right)^{-2} \left(\frac{\varepsilon_{\mathrm{peak}}}{100\ \mathrm{keV}}\right)^{-1} \left(\frac{\Gamma}{800}\right)^{2} \mathrm{eV}, \tag{18}$$

where we take $\delta = 2\Gamma$ as the Doppler factor, and $K_{p\gamma} = 0.2$. As shown in Asano et al. (2009a), a large Lorentz factor or a large radius R_0 is required in order to have GeV photons which escape unabsorbed from the source, and this leads to a lower photopion efficiency and a harder neutrino spectrum. Therefore, such models which result in GeV emission can avoid the GRB-neutrino upper limit constraints given by IceCube. Also, the report in Abbasi et al. (2012) excludes only GRB models with $\Gamma \lesssim 400$.

With the same method as for the neutrinos, we also plot the spectrum of the escaped neutrons without the GZK effect in Figure 9. The neutron energy range extends as far as the UHECR energy region, and the contribution from those 667 GRBs in this simple model seems close to the UHECR spectrum obtained with Auger (Abraham et al. 2010). The isotropic-equivalent energy of the neutrons escaped per burst (assuming $N = 30$ pulses) is 6.6×10^{51} erg, comparable to the energy emitted per burst (30 pulses) in γ-rays, 2×10^{52} erg. However, at 10^{20} eV the GZK effect is crucial so that we should count only GRBs within the GZK horizon (∼100 Mpc). The GRB rate within a 100 Mpc sphere (∼ the GZK horizon) becomes 8.4×10^{-3} GRBs yr^{-1} for the optimistic rate of 2 Gpc^{-3} yr^{-1} (Wanderman & Piran 2010). Here we simply assume that GRBs occur with this rate at a distance of 100 Mpc, and we plot the UHECR flux from those GRBs as the dashed line in Figure 9. Note that even though we adopt $\epsilon_p/\epsilon_e \simeq 12$, the energy fraction of escaped neutrons to gamma rays is ∼1/3, due to the larger radius and Γ leading to a modest $p\gamma$ rate. The UHECR flux level at 10^{20} eV is lower than the observed flux by a factor of ∼40, which implies that ten times the gamma-ray energy is required to be emitted as cosmic rays to make GRBs dominant sources of UHECRs. This is reconfirmation of the difficulty in the GRB-UHECR scenario pointed out in Eichler et al. (2010). Here we have taken the most pessimistic assumption for UHECR production, namely, that the high-energy protons cannot escape until they have cooled adiabatically. As a result, the escaped-neutron energy is a few percent of the injected energy of protons. Some mechanism to make protons escape may be required to produce UHECRs from GRBs. Of course, we also have to include the luminosity function, redshift distribution, and the uncertainties discussed in Waxman (2010). Such a detailed estimate of neutrinos and UHECR with our numerical simulations will be addressed in our future work.

4.2. Hadronic "Fermi-LAT" Case

Here we adopt a more specific parameter set that mimics a pulse of the bright GRBs observed with *Fermi*-LAT. The model parameters are $\Gamma = 600$, $R_0 = 1.3 \times 10^{16}$ cm, $E_{e,\mathrm{pls}} = 2.0 \times 10^{54}$ erg, and $E_{p,\mathrm{pls}} = 4.8 \times 10^{55}$ erg ($\epsilon_p/\epsilon_e \simeq 24$) including the acceleration effect after injection. The initial magnetic field $B'_0 = 830$ G is determined by the same method in Section 4.1 as $\epsilon_B/\epsilon_e = 3.0$ at $R = 2\ R_0$. The peak energy $\varepsilon_{\mathrm{peak}}$ is adjusted to be ∼1 MeV by adopting $\varepsilon'_{e,\mathrm{min}} = 13$ GeV.

The evolution of the particle spectra in the shell frame (Figure 10) is similar to that for the "moderate" case in Figure 4. However, the gamma-ray spectral bump above 10^7 eV is here attributed purely to hadrons. Although the ratio ϵ_B/ϵ_e is the same as that for the "moderate" case, the Klein–Nishina effect is crucial because of the very high $\varepsilon'_{e,\mathrm{min}}$. Therefore, the IC emission does not yield a spectral bump in this case. As the photon density increases, photons due to electromagnetic cascade triggered by photopion production appear above 10^7 eV.

Assuming $z = 4.35$, we plot the observer-frame spectral evolution in Figure 11. Initially ($t \leqslant 1.6$ s) the spectral shape is close to the simple Band function, and no spectral bump appears in the GeV energy range. In the later phase, the

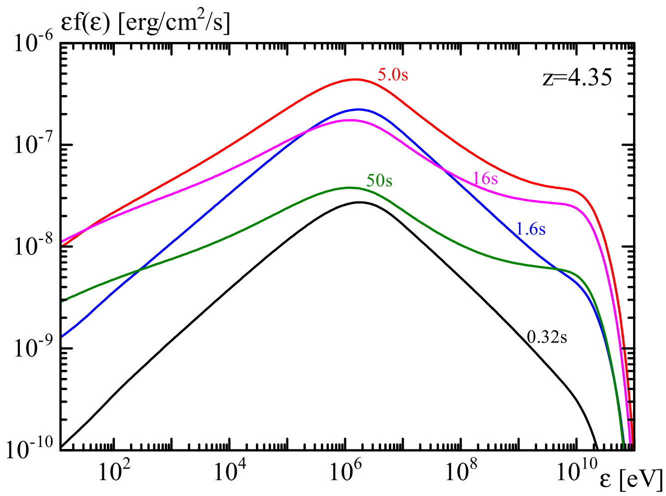

Figure 11. Hadronic "*Fermi*-LAT" case: flux evolution (see the text in Section 4.2) for an observer with $z = 4.35$.

(A color version of this figure is available in the online journal.)

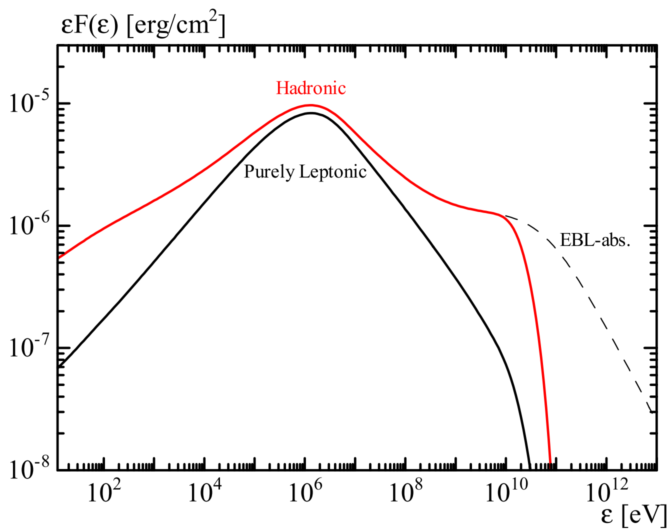

Figure 12. Fluences for the hadronic model and purely leptonic model ($\epsilon_p = 0$) with the "*Fermi*-LAT" parameters (see the text in Section 4.2) for an observer with $z = 4.35$. The dashed line is the spectrum without the absorption effect of the EBL.

(A color version of this figure is available in the online journal.)

hadronic component appears, and the entire shape gradually evolves into a flat one. This evolution is similar to the spectral behavior in GRB 080916C (Abdo et al. 2009c). The effect of the hadronic cascade on the spectral flatness is well shown in the time-integrated spectra in Figure 12. In contrast to this two-component hadronic behavior, the purely leptonic case for the same parameters leads to a pure Band-type time-integrated spectrum. The spectral shape is almost unchanged during the emission in the leptonic model.

The light curve in Figure 13 shows a significant delay of the 10 GeV light curve. The delay timescale (∼6 s) is comparable to the delay seen in GRB 080916C (Abdo et al. 2009c). In this case SSC is negligible, so the GeV spectral bump is purely due to hadronic cascade. Unlike in the "moderate case," the peak time of the 10 GeV photon light curve is here relatively close to the peak time for the neutrinos. Thus, the lack of SSC effects (moderated by the Klein–Nishina effect here) is of key importance in emphasizing the delayed onset in hadronic

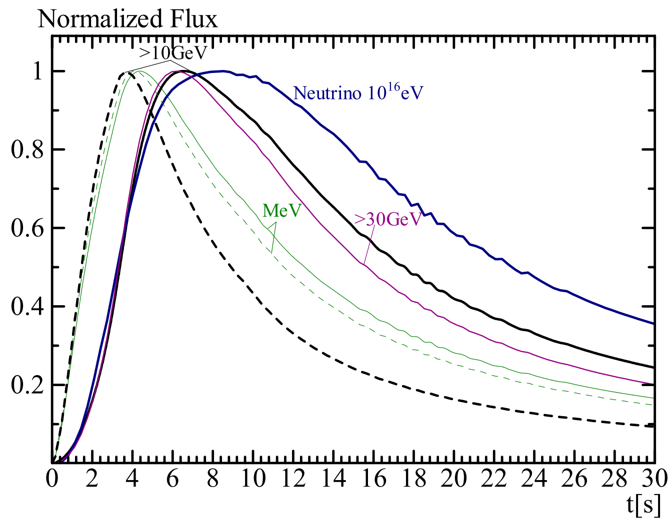

Figure 13. Light curves for the "*Fermi*-LAT" case with $z = 4.35$. See the text in Section 4.2. The designation of the labels is the same as that in Figure 8; full lines are for the hadronic model, dashed are for the purely leptonic one. In the hadronic model, since the 10–30 GeV photons originate mainly from the hadronic cascades, the peak times for those light curves and for the neutrino curve almost coincide with each other.

(A color version of this figure is available in the online journal.)

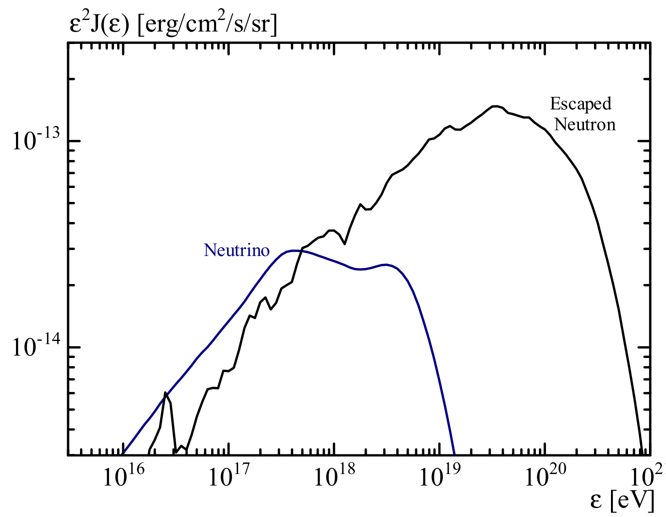

Figure 14. Spectra of the diffuse neutrons and neutrinos adopting a model with the "*Fermi*-LAT" hadronic cascade case (accumulating 10 GRBs yr^{-1}). See the text in Section 4.2.

(A color version of this figure is available in the online journal.)

models. The 10 GeV light curve shows a significantly broader FWHM (∼14 s) than the FWHM of the MeV light curve (∼11 s). In the same model without proton injection (dashed lines), the high-energy light curve is rather narrower than the MeV light curve. The onsets of the GeV and MeV light curves are almost simultaneous. Thus, for this parameter set, the difference between hadronic and leptonic models is prominent.

Here we have adopted a very large energy per pulse. In such cases the number of pulses may be a few, and the expected rate of such bright *Fermi*-LAT GRBs (in this example the fluence is 7.5×10^{-5} erg cm^{-2}) may be less than 10 per year. Thus, in the same manner as in Figure 9 adopting $N = 1$ and the rate 10 yr^{-1}, we plot the spectra of the neutrinos and neutrons due to bright *Fermi*-LAT GRBs in Figure 14. The spectrum of the escaped neutrons ranges as far as the UHECR energy scale

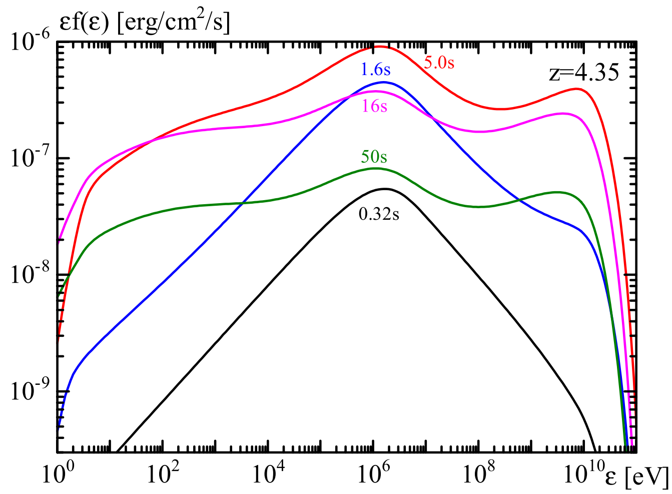

Figure 15. Proton synchrotron model: flux evolution (see the text in Section 4.3) for an observer with $z = 4.35$.

(A color version of this figure is available in the online journal.)

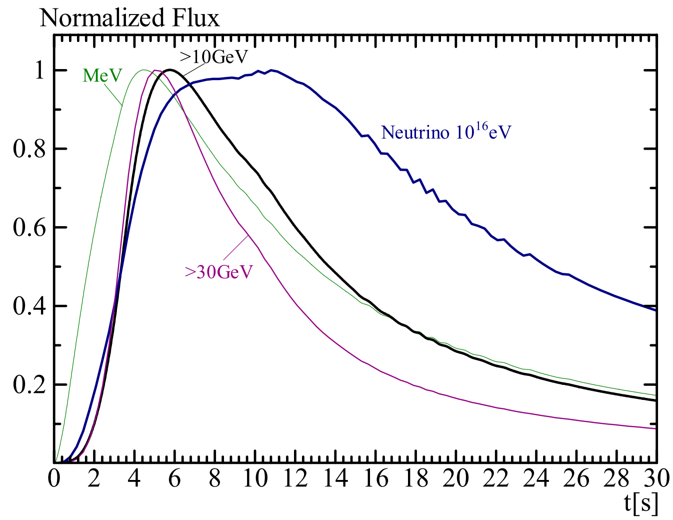

Figure 16. Proton synchrotron model: light curves observed from $z = 4.35$. See the text in Section 4.3. The designation of the labels is the same as that in Figure 8.

(A color version of this figure is available in the online journal.)

in this model also. The contributions to the diffuse neutrino background and to the integrated flux of escaping neutrons are smaller than in the "moderate case," owing to the low GRB rate with such parameters. However, the spectral flux of the neutrons at 10^{20} eV is comparable to that in the "moderate case," although such neutrons lose their energy by the GZK process. (Note that here we assumed $z = 4.35$, and the equivalent rate from within 100 Mpc would be much smaller than that for the "moderate" hadronic case parameters). The isotropic-equivalent energy of neutrons per pulse is 8.7×10^{53} erg, which is only 1.8% of the injected energy of protons, while the emitted isotropic-equivalent gamma-ray energy per pulse is 2.8×10^{54} erg.

The isotropic-equivalent energy of the neutrinos per pulse is 1.8×10^{53} erg. The break energy at $\sim 10^{17}$ eV in the neutrino spectrum is in apparent contradiction with Equation (18) for this parameter set. The reason is that in this case the pion production efficiency is not high enough, even for protons of $\gamma'_{\rm p} = \gamma'_{\rm p,th}$, the efficiency increasing as $\propto \gamma_{\rm p}^{0.5}$, as mentioned in Section 2. The neutron spectrum in the "*Fermi*-LAT" case in Figure 14 has a sharper peak at $\sim 3 \times 10^{19}$ eV than the "moderate" model of Figure 9. This indicates that only very high energy protons near the cutoff energy produce pions efficiently. The high-energy bump at $\sim 3 \times 10^{18}$ eV in the neutrino spectrum is attributed to pion decays from such high-energy protons/neutrons, while the low-energy break is attributed to the muon-decay component. Thus, also for this parameter set, the neutrino energy range is well above the energy range constrained by IceCube. The neutrino fluence ($\sim 10^{-6}$ erg cm^{-2}) from this pulse corresponds to $\sim 1/300$ of the IceCube limit (~ 0.2 GeV cm^{-2}; Abbasi et al. 2012).

4.3. *Proton Synchrotron*

A different hadronic model is the proton synchrotron model (Vietri 1995; Totani 1998; Razzaque et al. 2010). To test this case with the same Lorentz factor and initial radius as those in Section 4.2 we need to use extreme values for some of the other parameters, in order to ensure that proton synchrotron contributes to the GeV energy range. Thus, we adopt $E_{\rm e,pls} = 4.0 \times 10^{54}$ erg, and $E_{\rm p,pls} = 2.0 \times 10^{56}$ erg ($\epsilon_{\rm p}/\epsilon_{\rm e} = 50$), and the initial magnetic field $B'_0 = 4800$ G ($\epsilon_B/\epsilon_{\rm e} = 50$ at $R = 2\,R_0$). The minimum energy of electrons is set as $\varepsilon'_{\rm e,min} = 5.3$ GeV. If the acceleration parameter ξ for protons is unity, the maximum energy of protons in this strong magnetic field becomes too large and cascade emission from photopion production overwhelms the proton synchrotron emission. This is because the soft photon spectrum $\alpha \sim -1.5$ implies $f_{{\rm p}\gamma} \propto \gamma_{\rm p}^{0.5}$. In order to suppress photopion production, we degrade the maximum energy of protons by adopting $\xi = 100$.

The resultant spectral evolution for an observer at $z = 4.35$ is shown in Figure 15. Here the second peak of the photon spectra is due to proton synchrotron radiation. It is seen that proton synchrotron can produce harder spectra than the cascade emission seen in Figure 11. Even in this case, however, we cannot neglect photopion production. In the later phases, the spectrum becomes flat owing to the cascade triggered by photopions. The delay time of the 10 GeV light curve (Figure 16) is similar to that for the "*Fermi*-LAT" case. This is because the parameters Γ and R are common and the GeV bump is due to purely hadronic effects in both models. However, the FWHM of the 10 GeV light curve is narrower here and the decay timescale of the 10 GeV emission seems almost the same as the timescale in the MeV emission, while the 30 GeV light curve is narrower than the MeV light curve. This depends on the redshift or on model parameters (Γ etc.). However, for the proton synchrotron model, the pulse decay timescale roughly corresponds to the synchrotron cooling timescale, so that the decrease of the pulse timescale with photon energy may be a characteristic feature of such models. Although the degeneracy in the parameters is not easy to resolve, having an energy threshold as low as possible could help in distinguishing the previous "*Fermi*-LAT" hadronic cascade and this "*Fermi*-LAT" proton synchrotron model through their light curve differences.

The energy emitted as gamma rays, neutrons, and neutrinos per pulse is 9.0×10^{54} erg, 3.2×10^{54} erg, and 8.0×10^{53} erg, respectively. In Figure 17 we plot the spectra of the escaped neutrons and neutrinos in the same manner ($N = 1$, 10 GRBs yr^{-1}) as in Figure 14. The maximum energy of neutrons is suppressed by the large ξ (see Equation (13)). The neutron and neutrino spectral shapes are similar to those in Figure 14, although the typical energy ranges become lower. This is because the

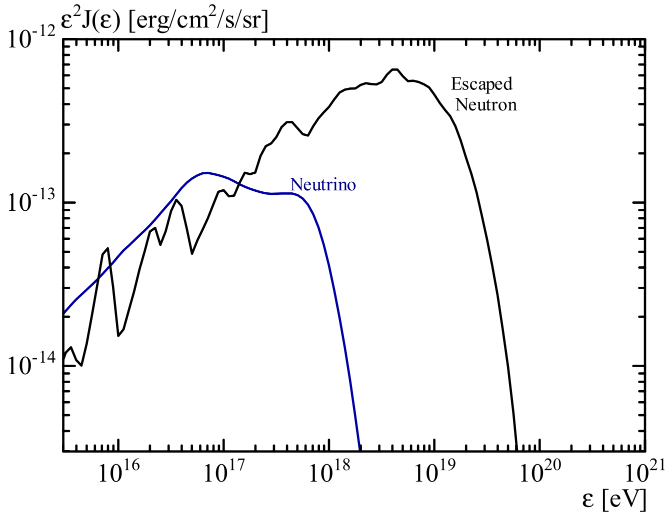

Figure 17. Spectra of the diffuse neutrons and neutrinos adopting a model with the "*Fermi*-LAT" proton synchrotron case. See the text in Section 4.3.

(A color version of this figure is available in the online journal.)

critical parameters for photopion production (R_0, Γ, and $E_{\rm e,pls}$) are almost the same in the two cases.

5. SUMMARY AND DISCUSSION

We have simulated the time evolution of the particle energy distributions in a relativistically expanding shell with parameters corresponding to those of GRBs observed by *Fermi*, and discussed the spectral evolution of the radiation seen in the observer frame. If we adopt a very weak magnetic field in the shell in a one-zone leptonic model, the slow evolution of the SSC emission due to the Klein–Nishina effect results in a delayed onset of the GeV emission, by amounts comparable to those observed by *Fermi*. However, in such leptonic models the FWHM of the GeV light curve is almost the same as that of the 0.1–1 MeV light curves, although the present-day low photon statistics in the GeV range makes it hard to compare the FWHMs. On the other hand, an EIC model, which is essentially a leptonic two-zone model, can reproduce the GeV delay naturally. A long tail for the GeV light curve, as shown in AM11, is possible evidence for this model. This can partially contribute to the extended GeV emission seen in several GRBs (see, e.g., Ghisellini et al. 2010). We have also tested the $\gamma\gamma$-opacity evolution effect with our code. At least in our one-zone formulation, an electron injection timescale longer than the expansion timescale is required in order to observe the opacity damping. The resultant light curves have a characteristic shape, and the growth of the cutoff energy is more gradual than in the current sample of *Fermi*-LAT bursts, which so far do not show a similar spectral evolution. Thus, $\gamma\gamma$-opacity evolution cannot be the reason for the delay.

The hadronic models studied here include both cascade models and a proton synchrotron model, both of which are able to reproduce the delayed onset with a delay timescale close to the pulse timescale ($\sim R_0/c\Gamma^2$). The delay is due to the long acceleration timescale of protons and continuous photopion production after the end of the particle injection. The wider FWHM for the GeV light curve than for the MeV light curve could be a signature of the hadronic cascade. If the Klein–Nishina effect prevents IC emissions, the delay due to hadronic cascade becomes more dominant. The numbers of escaped UHE neutrons in our examples are comparable to the gamma-ray energy. Since we have adopted large Γ and R values in order to simulate GRBs where GeV photons are able escape from the source, the resultant neutrino spectra are hard enough to avoid the current flux limit constraints from IceCube. In addition, as the *Fermi* team indicates (Ackermann et al. 2012), GRBs with extra components in the GeV band may be a small fraction of the GRB population. Therefore, even if GRBs accelerate UHE particles, the typical GRB parameters are in a range which implies a sufficiently low neutrino and GeV gamma-ray production efficiency. Our hadronic model also predicts a delayed onset of the neutrino emission, which is more pronounced than the corresponding GeV photon delay. If neutrinos are eventually observed, this may be another point which could be tested by future neutrino observations. The energy budget required for being UHECR sources appears insufficient in our examples. In future work, we plan to include the redshift evolution, luminosity function, and other details to further test the viability of the GRB-UHECR scenario.

The open problem of the low-energy photon spectral index α is not addressed in this paper. Here we inject the electrons in the usual manner; the minimum energy of the electrons at injection $\varepsilon'_{\rm e,min}$ being a free parameter.[4] The synchrotron cooling results in a soft effective electron distribution ($n'_{\rm e}(\varepsilon'_{\rm e}) \propto \varepsilon'^{-2}_{\rm e}$), so $\alpha \lesssim -1.5$ is unavoidable in this type of simulation. Spectral slopes such as these, while softer than the average $\alpha \sim -1$, are present in the BATSE database. Such softer slopes have the result of enhancing the photopion production efficiency, as well as the resultant flux of escaped neutrons. Note that here the energy fraction in protons required to generate a GeV extra component is not so high, $\epsilon_{\rm p}/\epsilon_{\rm e} = 10$–$25$ ($\sim f_e^{-1}$, in alternative notation), compared with the case of GRB 090510 where $\epsilon_{\rm p}/\epsilon_{\rm e} > 100$ was required to reconcile with the observed index $\alpha = -0.58$ (Asano et al. 2009a). Another consequence is that the soft spectra make it difficult to find a low-energy spectral excess in the X-ray region. In our hadronic examples, the low-energy excess appears in the later stages, when the power-law component due to the hadronic cascade becomes prominent or dominant over the entire spectrum. On the other hand, in order to have a self-consistent one-zone synchrotron model whether leptonic or hadronic, some mechanism to harden the spectrum (e.g., Asano & Terasawa 2009; Murase et al. 2012) would need to be included, which could change the light curves or the UHECR production efficiency.

In our simulations the minimum Lorentz factor of electrons at injection $\gamma'_{\rm e,min}$ is assumed, for simplicity, to be constant during the injection. Thus, our simulations do not show a significant $\varepsilon_{\rm peak}$ evolution, as seen in Figure 11, whereas an increase of $\varepsilon_{\rm peak}$ around the time of the GeV onset has been reported in GRB 080916C and 090902B. To reproduce such a $\varepsilon_{\rm peak}$ evolution in our model, a growth of $\gamma'_{\rm e,min}$ during the injection would need to be introduced. However, in GRB 090926A the $\varepsilon_{\rm peak}$ does not change drastically around the GeV onset time (Ackermann et al. 2011; Zhang et al. 2011). Given this variety of spectral evolution behaviors, at this stage one is unfortunately left without a definite guideline for including a temporal evolution of the model parameters.

In summary the GeV delays can be explained either by a one-zone leptonic model with very low magnetic field and high luminosity (AM11), or by normal parameter range one-zone

[4] As is well known, $\varepsilon'_{\rm e,min}$ is written by the phenomenological parameters: $\epsilon_{\rm e}$ and the number fraction of the accelerated electrons, both of which are not well constrained so far.

hadronic models (this work), or also by a normal magnetic field and luminosity two-zone leptonic model via EIC (Toma et al. 2009, 2010). However, the light curve behaviors of these models differ substantially from each other. The qualitative tendency of the multi-GeV light curves discussed here can be tested with future atmospheric Cerenkov telescopes such as CTA. For this purpose, it would be desirable that the low-energy threshold of those telescopes should be as low as possible, in order to ensure good photon statistics as well as the capability to observe the spectral evolution below the $\gamma\gamma$ cutoff energy due to EBL. Such an ideal instrument would provide the capabilities for significant breakthroughs in GRB physics.

First we appreciate the anonymous referee for valuable comments. This study is partially supported by Grants-in-Aid for Scientific Research No. 22740117 from the Ministry of Education, Culture, Sports, Science and Technology (MEXT) of Japan, and NSF PHY-0757155. We also thank the CTA consortium members, especially S. Inoue, K. Ioka, and M. Teshima.

REFERENCES

Abbasi, R., Abdou, Y., Abu-Zayyad, T., et al. 2012, Nature, 484, 351
Abdo, A. A., Ackermann, M., Ajello, M., et al. 2009a, Nature, 462, 331
Abdo, A. A., Ackermann, M., Ajello, M., et al. 2009b, ApJ, 706, L138
Abdo, A. A., Ackermann, M., Arimoto, M., et al. 2009c, Science, 323, 1688
Abraham, J., Abreu, P., Aglietta, M., et al. 2010, Phys. Lett. B, 685, 239
Ackermann, M., Ajello, M., Asano, K., et al. 2011, ApJ, 729, 114
Ackermann, M., Ajello, M., Baldini, L., et al. 2012, ApJ, 754, 121
Ackermann, M., Asano, K., Atwood, W. B., et al. 2010, ApJ, 716, 1178
Agostinelli, S., Allison, J., Amako, K., et al. 2003, Nucl. Instrum. Methods Phys. Res., Sect. A, 506, 250
Asano, K. 2005, ApJ, 623, 967
Asano, K., Guiriec, S., & Mészáros, P. 2009a, ApJ, 705, L191
Asano, K., & Inoue, S. 2007, ApJ, 671, 645
Asano, K., Inoue, S., & Mészáros, P. 2009b, ApJ, 699, 953
Asano, K., Inoue, S., & Mészáros, P. 2010, ApJ, 725, L121
Asano, K., & Mészáros, P. 2011, ApJ, 739, 103 (AM11)
Asano, K., & Nagataki, S. 2006, ApJ, 640, L9
Asano, K., & Takahara, F. 2003, PASJ, 55, 433
Asano, K., & Terasawa, T. 2009, ApJ, 705, 1714
Band, D., Matteson, J., Ford, L., et al. 1993, ApJ, 413, 281
Beloborodov, A. M. 2005, ApJ, 618, L13
Beloborodov, A. M. 2010, MNRAS, 407, 1033
Belmont, R., Malzac, J., & Marcowith, A. 2008, A&A, 491, 617
Bošnjak, Ž., Daigne, F., & Dubus, G. 2009, A&A, 498, 677
Böttcher, M., & Dermer, C. D. 1998, ApJ, 499, L131
Chodorowski, M. J., Zdziarski, A. A., & Sikora, M. 1992, ApJ, 400, 181
Corsi, A., Guetta, D., & Piro, L. 2010, A&A, 524, 92
Daigne, F., Bošnjak, Ž., & Dubus, G. 2011, A&A, 526, 110
Eichler, D., Guetta, D., & Pohl, M. 2010, ApJ, 722, 543
Ghisellini, G., Ghirlanda, G., Nava, L., & Celotti, A. 2010, MNRAS, 403, 926
Ghisellini, G., Guilbert, P., & Svensson, R. 1988, ApJ, 334, L5
Giannios, D., & Spruit, H. C. 2007, A&A, 469, 1
Gilmore, R. C., Bouvier, A., Connaughton, V., et al. 2012, arXiv:1201.0010
Granot, J., Cohen-Tanugi, J., & do Couto e Silva, E. 2008, ApJ, 677, 92
Gupta, N., & Zhang, B. 2007, MNRAS, 380, 78
Inoue, S., Granot, J., O'Brien, P., et al. (for the CTA Consortium) 2012, Astrop. Phys., submitted
Inoue, T., Asano, K., & Ioka, K. 2011, ApJ, 734, 77
Ioka, K. 2010, Prog. Theor. Phys., 124, 667
Jakobsson, P., Levan, A., Fynbo, J. P. U., et al. 2006, A&A, 447, 897
Kakuwa, J., Murase, K., Toma, K., et al. 2012, arXiv:1112.5940
Kaneko, Y., Preece, R. D., Briggs, M. S., et al. 2006, ApJS, 166, 298
Kneiske, T. M., Bretz, T., Mannheim, K., & Hartmann, D. H. 2004, A&A, 413, 807
Kumar, P., & Barniol Duran, R. 2010, MNRAS, 409, 226
Kumar, P., & Narayan, R. 2009, MNRAS, 395, 472
Li, Z. 2010, ApJ, 709, 525
Lithwick, Y., & Sari, R. 2001, ApJ, 555, 540
Mészáros, P. 2006, Rep. Prog. Phys., 69, 2259
Mészáros, P. 2012, Astrop. Phys., in press (arXiv:1204.1897)
Mizuno, Y., Pohl, M., Niemiec, J., et al. 2011, ApJ, 726, 62
Murase, K. 2008, Phys. Rev. D, 78, 101302
Murase, K., Asano, K., Terasawa, T., & Mészáros, P. 2012, ApJ, 746, 164
Murase, K., & Nagataki, S. 2006, Phys. Rev. D, 73, 3002
Murase, K., Toma, K., Yamazaki, R., & Mészáros, P. 2011, ApJ, 732, 77
Pe'er, A. 2008, ApJ, 682, 463
Pe'er, A., & Waxman, E. 2005, ApJ, 628, 857
Piran, T. 2005, Rev. Mod. Phys., 76, 1143
Preece, R. D., Briggs, M. S., Mallozzi, R. S., et al. 2000, ApJS, 126, 19
Razzaque, S., Dermer, C. D., & Finke, J. D. 2010, Open Astron. J., 3, 150
Rees, M. J., & Mészáros, P. 2005, ApJ, 628, 847
Ryde, F., Axelsson, M., Zhang, B. B., et al. 2010, ApJ, 709, L172
Toma, K., Wu, X.-F., & Mészáros, P. 2009, ApJ, 707, 1404
Toma, K., Wu, X.-F., & Mészáros, P. 2010, MNRAS, 415, 1663
Totani, T. 1998, ApJ, 509, L81
Vietri, M. 1995, ApJ, 453, 883
Vurm, I., & Poutanen, J. 2009, ApJ, 698, 293
Wanderman, D., & Piran, T. 2010, MNRAS, 406, 1944
Waxman, E. 1995, Phys. Rev. Lett., 75, 386
Waxman, E. 2010, arXiv:1010.5007
Waxman, E., & Bahcall, J. 1997, Phys. Rev. Lett., 78, 2292
Waxman, E., & Bahcall, J. 1998, Phys. Rev. D, 59, 023002
Zhang, B.-B., Zhang, B., Liang, E.-W., et al. 2011, ApJ, 730, 141
Zhang, W., MacFadyen, A., & Wang, P. 2009, ApJ, 692, L40